Bioactive Materials 6 (2021) 4625–4639

Contents lists available at ScienceDirect

Bioactive Materials

journal homepage: www.sciencedirect.com/journal/bioactive-materials

Magnetic field-mediated Janus particles with sustained driving capability for severe bleeding control in perforating and inflected wounds

Qing Li [a,b,1], Enling Hu [a,b,1], Kun Yu [a,b], Mengxing Lu [a,b], Ruiqi Xie [a,b], Fei Lu [a,b], Bitao Lu [a,b], Rong Bao [c], Guangqian Lan [a,b,*]

[a] State Key Laboratory of Silkworm Genome Biology, College of Sericulture, Textile and Biomass Sciences, Southwest University, Chongqing, 400715, China
[b] Chongqing Engineering Research Center of Biomaterial Fiber and Modern Textile, Chongqing, 400715, China
[c] The Ninth People's Hospital of Chongqing, No. 69 Jialing Village, BeiBei District, Chongqing, 400715, China

ARTICLE INFO

Keywords:
Janus particle
Sustained driving
Magnetic guidance
Hemostasis
Complex wound

ABSTRACT

Severe bleeding in perforating and inflected wounds with forky cavities or fine voids encountered during prehospital treatments and surgical procedures is a complex challenge. Therefore, we present a novel hemostatic strategy based on magnetic field-mediated guidance. The biphasic Janus magnetic particle (MSS@Fe_2O_3-T) comprised aggregates of α-Fe_2O_3 nanoparticles (Fe_2O_3 NPs) as the motion actuator, negatively modified microporous starch (MSS) as the base hemostatic substrate, and thrombin as the loaded hemostatic drug. Before application, the particles were first wrapped using $NaHCO_3$ and then doped with protonated tranexamic acid (TXA-NH_3^+), which ensured their high self-dispersibility in liquids. During application, the particles promptly self-diffused in blood by bubble propulsion and travelled to deep bleeding sites against reverse rushing blood flow under magnetic guidance. *In vivo* tests confirmed the superior hemostatic performance of the particles in perforating and inflected wounds ("V"-shaped femoral artery and "J"-shaped liver bleeding models). The present strategy, for the first time, extends the range of magnetically guided drug carriers to address the challenges in the hemorrhage control of perforating and inflected wounds.

1. Introduction

Uncontrolled hemorrhage caused by severe injuries in the military battlefield or during accidents remains a major global concern because it increases the patient's risk of mortality due to hemorrhagic shock coagulopathy, infection, and multiple organ failure [1]. Conventional hemostatic strategies such as mechanical bandaging may fail to stop severe bleeding during prehospital treatments [2]. This is because hemostatic materials that provide a barrier to rapidly seal the hemorrhage cavity and prevent excessive blood flow from the wound may insufficiently coagulate blood [3]. Moreover, uncompressible bleeding in perforating and inflected wounds, caused by sharp tools or small-bore weapons and characterized by inflected internal shapes and bleeding sites that may be deep, complex, and difficult to identify, poses further challenges for hemostasis and ultimately leads to serious injuries and fatalities [4].

Various commercial hemostatic materials, such as a modified cellulose-based hemostatic product (Surgicel®) [5], zeolite-based styptic agent (QuikClot®) [6], clay-based hemostatic agent (WoundStat®) [7], and chitosan-based hemostatic product (Celox™), are currently available for hemorrhage control [8], Although these commercial materials are capable of controlling excessive bleeding, they fail to halt severe hemorrhage in perforating and inflected wounds [9], This is because these hemostatic agents typically exert their effects only on the wound surface or the exported bleeding hemocoel but are incapable of reaching deep and secluded bleeding sites. Therefore, there has been a lack of adequate hemostatic agents that are effective at coagulating blood in hemocoels at deep and secluded bleeding sites, and the control of excessive bleeding has been unsuccessful.

To address these issues, novel hemostatic materials that exert their effects by physical plugging or sealing of the bleeding chamber at deep bleeding sites have been developed [10–12]. In particular, volume-expansion hemostatic foams have attracted widespread interest

Peer review under responsibility of KeAi Communications Co., Ltd.
* Corresponding author. State Key Laboratory of Silkworm Genome Biology, College of Sericulture, Textile and Biomass Sciences, Southwest University, Chongqing, 400715, China.
E-mail address: 30353930@qq.com (G. Lan).
[1] Equally contributed.

https://doi.org/10.1016/j.bioactmat.2021.05.006
Received 29 January 2021; Received in revised form 30 April 2021; Accepted 3 May 2021

owing to their fast liquid-absorbing capacity and shape recovery/expansion properties [13]. As reported, after they are plugged or pushed into the bleeding cavity, these foams rapidly absorb blood and undergo shape recovery/expansion to fit the bleeding wound cavity [14]. Blood coagulation, therefore, occurs rapidly inside the hemocoel for efficient hemostasis. However, these volume-expansion foams may fail to reach specific deep and secluded bleeding sites. The macroscopic form and solid structure of the foams limit widespread contact between the hemostatic agent and the fine ravines or voids in the bleeding cavity. Insufficient adaptation with hemorrhagic hemocoels results in free bleeding sites and markedly prolongs the hemostasis time. Furthermore, rough plugging or pushing may aggravate hemorrhage, while excessive expansion or postoperative removal of foams from the wounds may increase the risk of secondary bleeding.

To facilitate contact between the hemostatic agent and the deep and secluded bleeding sites, active motion-mediated hemostatic agents have been proposed [15]. Bubble-driven hemostatic powders easily enter the hemorrhage cavity and self-drive into deep and secluded bleeding sites against rapid and excessive blood flow. As a result, blood coagulation is first activated in the bleeding sites and then extends to the entire wound chamber. Nevertheless, this approach has several limitations. First, the non-direction-selective motion of powder hemostatic agents leads to decreased utility because some powder hemostatic agents do not drive into deep bleeding sites but may either move sideways or drive to an inadequate depth. Second, the gas bubbles generated around the carrier may cause counteractions or a reciprocal decrease in propelling force, thereby limiting the self-driving efficiency of these hemostatic particles. Third, the hemostatic powder (calcium carbonate as the main substrate) lacks blood absorption ability or a cell aggregation matrix, which leads to reduced hemostatic efficiency.

To tackle the above issues, we developed a direction-selective motion strategy for powder hemostatic agents [16]. Specifically, $CaCO_3$, which acts as a gas generator, was asymmetrically formed on one side of the microporous starch particles. These dual-component particles, termed Janus hemostatic particles because of their asymmetric structure, localize the driving power at a specific area rather than evenly distributing it over the entire substrate [17,18]. Thus, the Janus hemostatic particles are able to self-drive deeper against reverse-rushing blood flow. However, several factors of the bubble-driving strategy require consideration because the durability of *in situ* bubble generation may significantly affect the motion performance of the hemostatic powder. First, the driving bubbles are generated from the reaction between protonated tranexamic acid (TXA-NH_3^+) and $CaCO_3$, which are both components of the hemostatic particles. Therefore, the efficiency and durability of bubble generation are subject to the loading percentage of TXA-NH_3^+ and $CaCO_3$. Consequently, the driving forces applied over the hemostatic powder may be nondurable or inadequate as the loading percentage cannot be increased in an unlimited manner. To address this issue, alternative driving/guidance strategies are required to enhance the durability of the motion behavior of powder hemostatic agents.

One potential strategy involves the use of a magnetic field as the power source to provide sustained and strong mobility. Iron oxide nanoparticles (Fe_2O_3 NPs) have gained substantial interest in biomedical applications, such as drug delivery [19], cancer therapy [20], and magnetic diagnostic imaging [21], because they exhibit excellent magnetic controllability, hyperthermia performance, and biocompatibility [22,23]. Fe_2O_3 NPs are particularly useful for treating intravascular and intracranial tumors, which are highly covert and are difficult to treat using conventional operations. Qian et al. recently prepared an injectable magnetic hydrogel containing Fe_2O_3 NPs to provide effective magnetic hyperthermia in the deep and covert sites of hepatocellular carcinoma [24], while Singh et al. designed an Fe_2O_3 NPs-containing robot to deliver drugs *via* magnetic field guidance [25]. These studies confirmed the universality and safety of Fe_2O_3 NPs and the feasibility of magnetic field-guided drug delivery in cancer therapies. Among the magnetic field-guided drug carriers used in cancer therapies, Fe_2O_3 NPs can be synthesized by unilateral *in situ* growth on the porous particle substrate that carry the drug [26]. The dual phasic Janus particle comprises a base substrate that carries the drug (phase I) and Fe_2O_3 NPs (phase II); this structure is similar to that of the particles reported in our previous work [16]. By combining the two different phases, the Janus particles can be driven controllably and persistently guided by the applied magnetic field acting on the Fe_2O_3 NPs and drugs can be released at bleeding sites from the microporous drug-carrying phase [27]. The introduction of magnetic field-mediated nanoparticles to hemostatic Janus particles may facilitate the development of a controllable hemostatic motor with sustained and strong mobility, thus enabling access to the bleeding sites located inside perforating and inflected wounds for hemostasis.

In this regard, we aimed to develop a novel hemostatic particle with a Janus structure based on negatively charged microporous starch (MSS) and magnetic field-mediated α-Fe_2O_3 nanoparticles (Fe_2O_3 NPs) that are biocompatible and have been widely used in bioengineering. The Fe_2O_3 NPs were first assembled unilaterally on MSS to form magnetic field-guidable particles (MSS@Fe_2O_3). Then, thrombin, a hemostatic molecule used clinically [28], was loaded onto the as-prepared particles to form thrombin-carrying particles (MSS@Fe_2O_3-T), thus ensuring efficient coagulation at bleeding sites. Since starch particles aggregate easily in liquids, which may substantially decrease the efficiency of the Janus hemostatic particle, a self-dispersing strategy based on bubble propulsion was proposed to ensure that MSS@Fe_2O_3-T are evenly distributed in blood upon contact. Specifically, $NaHCO_3$ was first coated on MSS@Fe_2O_3-T to form alkali-enveloped particles (MSS@Fe_2O_3-T--$NaHCO_3$), which were then doped with acidic TXA-NH_3^+ to form the final products for hemostasis. When the particles come into contact with water/blood, alkaline and acidic donors ($NaHCO_3$ and TXA-NH_3^+, respectively) immediately react to generate numerous CO_2 microbubbles, allowing the Janus particle MSS@Fe_2O_3-T to self-diffuse by bubble propulsion. Therefore, magnetic field-mediated Janus particles are assumed to reach deep bleeding sites and induce the coagulation cascade to control severe hemorrhage in perforating and inflected wounds (Fig. S1). This study is the first to apply magnetic guidance to drug carriers for hemostasis. This novel strategy is expected to augment the direction-selective motion of particle hemostatic agents in reverse blood flow, leading to enhanced hemostasis in perforating and inflected wounds.

2. Results and discussion

Preparation and characterizations. Magnetic Janus particles (MSS@Fe_2O_3) were synthesized according to a magnetic field-guided method involving negatively charged MSS as the substrate, α-Fe_2O_3 nanoparticles (Fe_2O_3 NPs) as the magnetic source, and cetyltrimethyl ammonium bromide (CTAB) as the template (Fig. 1A). The positive potential of CTAB ensured the occurrence of the assembling reaction around MSS during preparation. Magnetic field guidance provided a targeted force on the Fe_2O_3 NPs, which resulted in uniaxial assembling of these magnetic nanoparticles on MSS. The aggregation of Fe_2O_3 NPs strengthened with time, increasing in the aging process accompanied by magnetic field guidance. After the removal of CTAB, a series of magnetic Janus particles with different Fe_2O_3 NP contents were obtained. The optical microphotographs shown in Fig. 1B depict the Janus contour shape of these particles. The dark region indicates Fe_2O_3 aggregation, which shows a compact and solid structure. With an increase in the feeding mass ratio of MSS to Fe_2O_3, the compositional ratio of the Fe_2O_3 aggregates in these Janus particles increased from 4.6% to 60.3% (Fig. 1C); at the same time, the corresponding size of Fe_2O_3 aggregates increased to 15.7 μm (Fig. 1B). This indicated that not all Fe_2O_3 NPs contributed to the formation of Fe_2O_3 aggregates. In addition, stability evaluation suggested that the particle size was maintained when it was stored at 37 °C for 4 weeks (Fig. S2).

A high feeding mass of Fe_2O_3 NPs resulted in a surplus; these

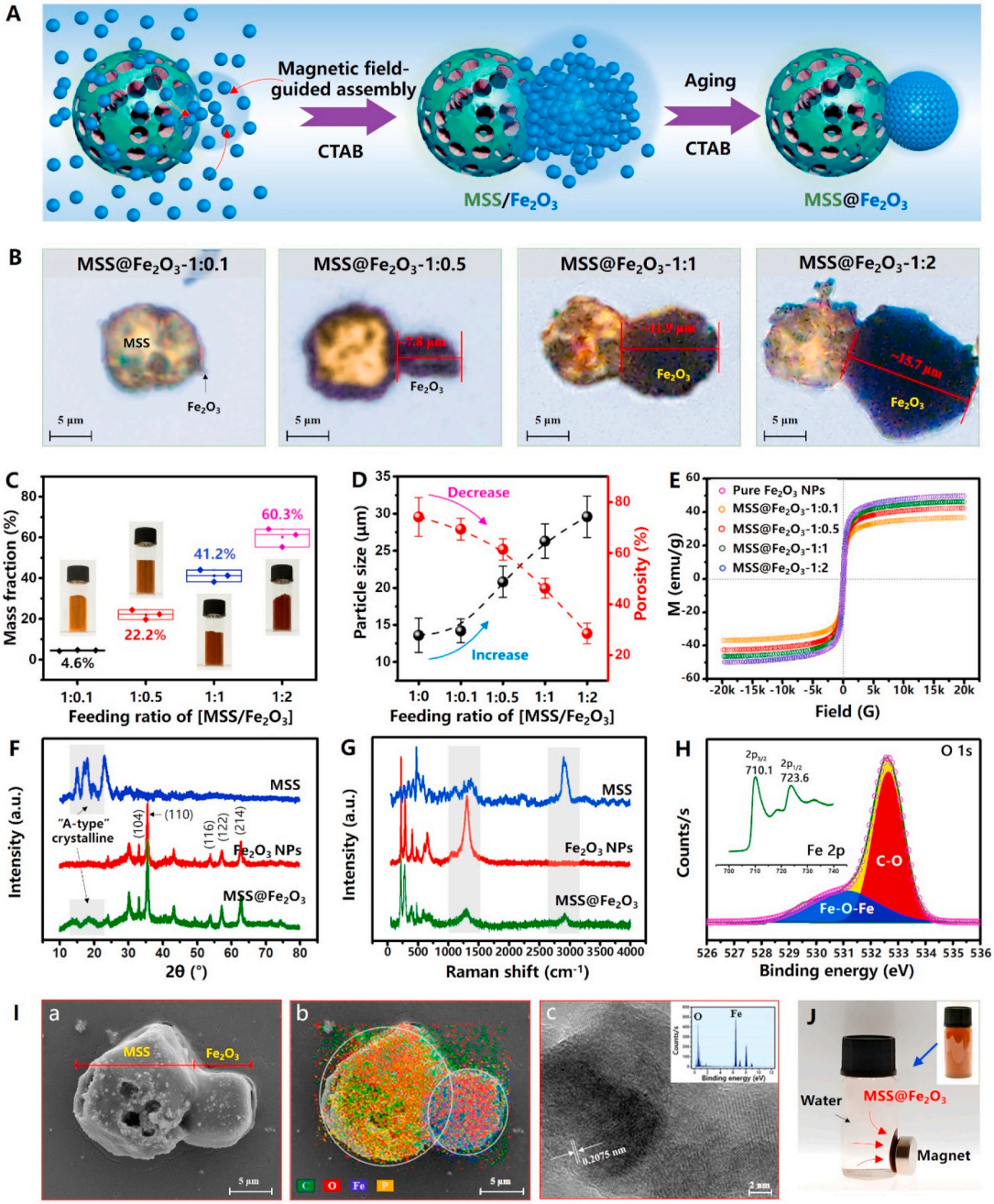

Fig. 1. A) Schematic of the synthesis of Janus MSS@Fe_2O_3 particles. B) Optical microphotographs of various MSS@Fe_2O_3 particles prepared in different feeding ratios. C) Mass fraction of Fe_2O_3 NPs from various MSS@Fe_2O_3. D) Particle size and porosity of MSS@Fe_2O_3. E) Magnetization curves at 300 K. F) X-ray diffraction (XRD) analysis of typical materials. G) Raman spectra of typical materials. H) X-ray photoelectron spectroscopy (XPS) spectra of MSS@Fe_2O_3 (feeding ratio of [MSS]/[Fe_2O_3 NPs]: 1:1. I) Electron microscopy images of MSS@Fe_2O_3: (a) Scanning electron microscopy (SEM) and its corresponding (b) mapping images and (c) transmittance electron microscopy (TEM) of Fe_2O_3 NPs from MSS@Fe_2O_3. Inset shows the energy disperse spectroscopy (EDS) analysis. J) Magnetic guidance of MSS@Fe_2O_3 particles in water.

particles were dispersed in the reaction solution, filled the pores of MSS, or attached to the apparatus. This resulted in an increase in size and magnetism but a decrease in the porosity of MSS@Fe_2O_3 (Fig. 1D). Sufficient porosity of the hemostatic particles plays a vital role in blood absorption and blood cell aggregation [29], which determines successful hemostasis. The porosity decreased slightly from 74.2 ± 7.6% to 69.4 ± 4.3% compared to that of MSS, but it was still adequate for use as a hemostatic agent. Since MSS@Fe_2O_3 equipped with Fe_2O_3 aggregates of 7.8 μm in diameter exhibited superior superparamagnetic property (Fig. 1E) and good magnetic stability (Fig. S3), it was selected for subsequent characterization and evaluation of magnetic motion and hemostatic ability.

The composition and structure of as-synthesized MSS@Fe_2O_3 were confirmed by X-ray diffraction (XRD), Raman spectroscopy, and X-ray photoelectron spectroscopy (XPS). Peaks in the range of 14°–18° revealed the characteristic "A-shape" of crystalline corn starch for MSS [30], as shown in Fig. 1F. In the spectra of Fe_2O_3 NPs and MSS@Fe_2O_3, peaks were detected at 33.2°, 35.6°, 54.1°, 57.4°, and 62.8°, corresponding to the α-Fe_2O_3 NP planes of (104), (110), (116), (122), and (214), respectively (JCPDS card no. 33–0064) [31]. The Raman spectrum of MSS@Fe_2O_3 exhibited the characteristic peaks of MSS and Fe_2O_3 NPs, confirming the coexistence of the two components (Fig. 1G).

Further valence state analysis for MSS@Fe_2O_3 is presented in Fig. 1H. An O 1s spectrum at 527–535 eV was detected and fitted with two different peaks. The fitted peak with a high binding energy of 532.6 eV was attributed to C–O in MSS, and the other fitted peak was assigned to the O^{2-} ions (Fe–O–Fe) in the Fe_2O_3 aggregates. Two characteristic peaks at 710.1 and 723.6 eV in the Fe 2p spectrum were observed for the Fe_2O_3 aggregates, corresponding to Fe $2p_{3/2}$ and Fe $2p_{1/2}$, respectively [32]. The distinct biphasic structure of MSS@Fe_2O_3 was confirmed by high-definition scanning electron microscopy (SEM), as shown in Fig. 1Ia. The corresponding mapping image in Fig. 1Ib showed that Fe aggregated predominantly in the smaller spherical region, corresponding to the solid Fe_2O_3 aggregation phase. The P element was apparent only in the bigger spherical region, which corresponded to the MSS phase. The transmission electron microscopy (TEM) image and energy disperse spectroscopy spectrum shown in Fig. 1I(c) provide evidence for the aggregation of Fe_2O_3 NPs (10 nm) in MSS@Fe_2O_3. In addition, the lattice spacing for Fe_2O_3 NPs was 0.2075 nm, consistent with the data reported in a previous study [33]. These results confirmed the Janus structure of MSS@Fe_2O_3 with two components: MSS and Fe_2O_3 aggregates.

Examination of Magnetic Field-Mediated Motion Behavior. The presence of Fe_2O_3 endowed MSS@Fe_2O_3 with excellent magnetic properties. MSS@Fe_2O_3 was rapidly actuated to aggregate under the influence of a magnetic field (Fig. 1J) and travelled easily in static water following the motion trails of the magnet (Fig. 2A and B, and Movie S1). In addition, the magnetic field-mediated driving behavior of

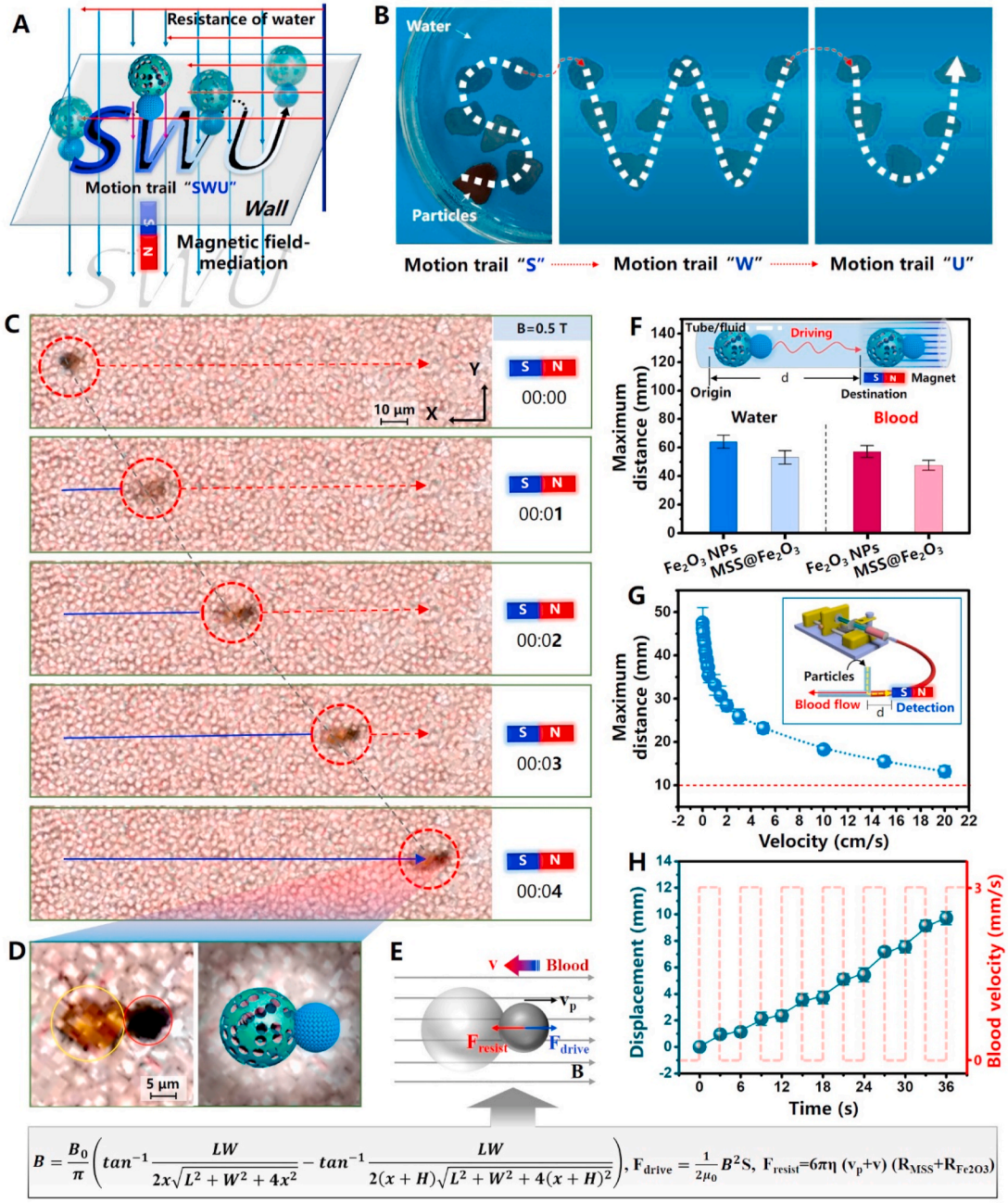

Fig. 2. A) Schematic of the magnetic driving behavior of MSS@Fe_2O_3. B) Driving behavior of MSS@Fe_2O_3 in static water. C) Microphotographs of the magnetic driving of MSS@Fe_2O_3 in static citrated blood. D) MSS@Fe_2O_3 and its schematic. E) Horizontal force analysis on MSS@Fe_2O_3. The maximum horizontal magnetic induction distance of MSS@Fe_2O_3 in F) static water and blood and G) flowing blood. H) Horizontal displacement of MSS@Fe_2O_3 against periodic blood impulses (3 s per cycle with a velocity of 3 cm s^{-1}).

MSS@Fe_2O_3 in static blood was investigated. As shown in Fig. 2C and Movie S2, the MSS@Fe_2O_3 particles moved rapidly owing to the magnetic field-mediated Fe_2O_3 aggregates (dark region). The viscous resistance of blood only weakly impeded the forward motion in the presence of magnetic forces. For the force analysis, the Janus MSS@Fe_2O_3 particles were modeled as two conterminous solid spheres (Fig. 2D and E). The bigger sphere corresponded to MSS, while the smaller one represented the Fe_2O_3 aggregates. The magnetic field at Fe_2O_3 provided the driving force, F_{drive}, for the entire particle (MSS@Fe_2O_3), which was calculated according to Equation (1):

Supplementary data related to this article can be found at https://doi.org/10.1016/j.bioactmat.2021.05.006.

To reduce the calculation errors caused by magnetic flux leakage, the magnetic field strength formula was employed to deduce B, which can be calculated according to Equation (2):

$$B = \frac{B_0}{\pi}\left(\tan^{-1}\frac{LW}{2x\sqrt{L^2+W^2+4x^2}} - \tan^{-1}\frac{Lw}{2(x=H)\sqrt{L^2+W^2+4(x+H)^2}}\right) \quad (2)$$

where B_0 is the magnetic field strength of the external magnet (0.5 T), x is the distance of MSS@Fe_2O_3 away from the magnetic induction surface center, and L, W, and H are the length, width, and thickness of the magnet, respectively (8, 6, and 1.5 cm, respectively).

Because MSS@Fe_2O_3 was modeled as two conterminous solid spheres (MSS and Fe_2O_3 aggregates), the overall resistance force (F_{resist}) of blood that affected MSS@Fe_2O_3 could be divided into two parts: force on MSS ($F_{MSS_{resist}}$) and force on Fe_2O_3 ($F_{Fe2O3_{resist}}$). The Reynolds number in the system ranged from 1 to 100 according to previous studies [15,34]; thus, F_{resist} was calculated according to Equation (3):

$$F_{resist} = 6\pi\eta\ (v_p + v)\ (R_{MSS} + R_{Fe2O3}) \quad (3)$$

where η is the viscosity of blood flow (2×10^{-3} Pa·s), v_p and v are respectively the speed of particle and blood, and R_{MSS} and R_{Fe2O3} are respectively the radii of the modeled MSS sphere and Fe_2O_3 sphere.

F_{drive} depends on the distance (x) between the particles and the external magnet, and F_{resist} mainly depends on the velocity of blood. Thus, an increase in blood velocity resulted in an increase in blood resistance to MSS@Fe_2O_3. When the resistance increased over the driving force ($F_{resist} > F_{drive}$), MSS@Fe_2O_3 hardly moved forward even after actuation. Thus, to overcome resistance from blood flow, enlarged magnetic actuation force applied on the MSS@Fe_2O_3 was necessary for driving the particles forward. To investigate the drive capacity of MSS@Fe_2O_3 in a constant magnetic field (B = 0.5 T), the maximum magnetic induction distance in water or blood was detected, as depicted in Fig. 2F–H. The horizontal maximum magnetic induction distances for MSS@Fe_2O_3 in water and blood were 53.2 ± 4.7 and 47.6 ± 3.5 mm, respectively (Fig. 2F), which are close to those of pure Fe_2O_3 NPs. This result was in agreement with the results of VSM evaluation (Fig. 1E), highlighting the strong magnetic properties of MSS@Fe_2O_3. Further measurements of the horizontal driving capacity of MSS@Fe_2O_3 were conducted using a self-constructed fluid device. As shown in Fig. 2G, the horizontal maximum distance (d) of the magnetic response decreased gradually from 47.6 ± 3.5 mm to 13.2 ± 1.3 mm when the blood flow speed increased (from 0 to 20 cm s^{-1}). The decrease in maximum magnetic response distance was most evident in velocity, which ranged from 0 to 3 cm s^{-1}, whereby the distance significantly dropped from 47.6 ± 3.5 mm to 25.9 ± 1.7 mm. As the velocity increased beyond 3 cm s^{-1}, the decline in the maximum magnetic response distance slowed down. In addition, as the periodic rhythm of muscular movements caused by respiration may influence blood flow behavior, magnetic driving performance against dynamic blood was further evaluated. The periodic impact of flowing blood was mimicked by setting the blood impulse cycle to 3 s [27]. Fig. 2H shows the forward horizontal movement of MSS@Fe_2O_3 in dynamic blood flow at a speed of 3 cm s^{-1} with cyclic impulse. No stagnation (indeclinable value) or reflux (reduced value) behavior was detected, suggesting that abrupt changes in blood flow would not stop MSS@Fe_2O_3 driving. Instead, these magnetic particles moved forward with almost stable velocity, regardless of blood impulse.

Similarly, the magnetic driving behavior of MSS@Fe_2O_3 in the vertical direction was also evaluated. As shown in Fig. 3A–C, the evolution trends of related behaviors in the vertical direction were in line with those of the horizontal direction. In addition, the maximum magnetic distance detected for MSS@Fe_2O_3 against the vertical flow of blood was higher than that against the horizontal flow of blood. This may be attributed to the effect of gravity on the particles. These results underscore the excellent magnetic field-mediated driving capacity of MSS@Fe_2O_3, highlighting the potential as carriers of hemostatic drugs to hemorrhage sites.

Starch particles possess good viscous and deformable properties [35] and can effectively block hemorrhage sites upon contact with blood. To investigate the blood-blocking capacity of starch-based MSS@Fe_2O_3, a self-constructed fluid control device was used as a simulative bleeding wound (Fig. S4). The bleeding wound model was fixed on a magnet and connected to a syringe pump that induces blood to mimic hemorrhage through a transport tube (tube A). When injected into tube A, blood was channeled into tubes B and C. The blood liquid level in the "bleeding cavity" was equal to that in tube B due to barometric pressure. After the applying particles into the "bleeding cavity," only blood outflow through tube B would indicate successful hemorrhage control in the "bleeding cavity"; in contrast, blood outflow through tube D would indicate failure of hemorrhage control. Thus, the blood flowing behavior in tubes B and D could be used to indicate the blocking capacity of MSS@Fe_2O_3.

With blood flowing into the cavity at a velocity of 3 cm s^{-1}, neither Celox™ (Fig. 3D and Movie S3) nor MSS (Fig. 3E, and Movie S4) was able to coagulate blood, because blood was observed to be flowing through Tube D. A similar phenomenon was observed when pure Fe_2O_3 NPs were used (Fig. 3F). Although Fe_2O_3 NPs were actuated immediately and adhered tightly to the bottom of the cavity, the aggregates formed were not robust enough to prevent the dynamic blood flow into tube D (Fig. 3F and Movie S5). However, successful hemostasis was achieved in 18.4 ± 3.4 s after application of MSS@Fe_2O_3, as blood outflow was through tube B only (Fig. 3G and Movie S6). In addition, there were no significant adverse effects of cyclic blood impulse on the blood-blocking capacity of MSS@Fe_2O_3, although the blocking time was slight longer (29.5 ± 6.2 s), as shown in Fig. 3H.

Supplementary data related to this article can be found at https://doi.org/10.1016/j.bioactmat.2021.05.006.

The velocity of blood flow and the quantity of the applied particles were varied to investigate their impact on the blood-blocking capacity of MSS@Fe_2O_3. As shown in Fig. 3I, increasing the blood flow velocity from 0 to 3 cm s^{-1} resulted in an increase in blocking time; in contrast, an increase in particle amount led to shortened blocking times. The excellent blocking ability in *in vitro* bleeding models may be attributed to the synergistic effects of the MSS base substrate and its loaded magnetic Fe_2O_3 aggregates. First, magnetic mediation of the Fe_2O_3 aggregates ensured that MSS@Fe_2O_3 accumulated densely at or close to the mimicked bleeding sites; then, MSS with good viscous and deformable properties enabled MSS@Fe_2O_3 to form a solid-like barrier to block the bleeding cavity tightly [Fig. 3G(c)]. Therefore, the excellent blocking capacity against bleeding models *in vitro* highlighted the feasibility of MSS@Fe_2O_3 in hemorrhage control in perforating and inflected wounds *in vivo*.

Examination of Hemophagia and Rheological Properties. MSS preserves high porosity and roughness, and its large specific area enables effective water and blood absorption. Therefore, despite the low hydrophilic and hemotropic properties of Fe_2O_3 NPs, integration of MSS with Fe_2O_3 NPs ensured MSS@Fe_2O_3 composites with good hydrophilic and hemotropic properties [Fig. 4A(a)] and almost equivalent water and

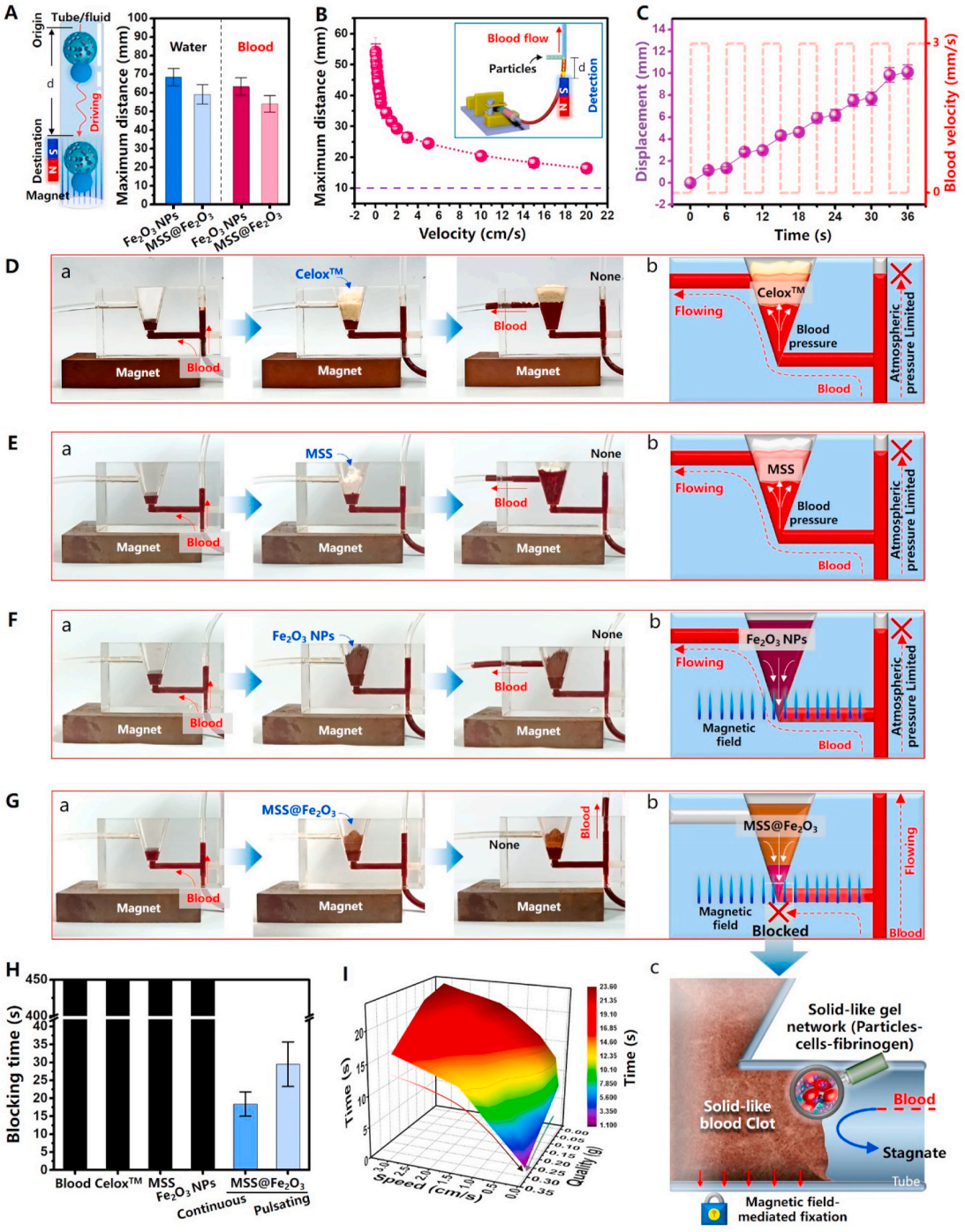

Fig. 3. Maximum vertical magnetic induction distance of MSS@Fe_2O_3 in A) static water and blood and B) flowing blood. C) Horizontal displacement of MSS@Fe_2O_3 against periodic blood impulses (3 s per cycle at a velocity of 3 cm s^{-1}). Blood-blocking behavior of D) Celox™, E) MSS, F) Fe_2O_3 NPs, and G) MSS@Fe_2O_3 in *in vitro* hemorrhage models. a) Photographs and b) schematic of the blocking process. c) Schematic of MSS@Fe_2O_3 halting in the model. H) Blocking time in *in vitro* hemorrhage models. I) Effects of the quantity of MSS@Fe_2O_3 and blood flow velocity on blocking time.

blood absorption capacity as that of MSS [Fig. 4A(b)]. To observe fluxion behavior, blood mixed with various amounts of MSS@Fe_2O_3 (from 100 to 1100 mg mL^{-1}) was poured into a round-bottomed container, which was then tilted ($\theta = 45°$). After applying a sufficient amount of MSS@Fe_2O_3, liquid blood turned to a solid-like clot gradually, depending on the amount of MSS@Fe_2O_3, which was in line with the finding of a previous study [36]. Phase transition of liquid blood occurred when MSS@Fe_2O_3 aggregated and interacted with water in the blood, thereby forming a solid-like clot with a protein-starch gel network. As shown in Fig. 4B, an MSS@Fe_2O_3 dosage of 800 mg mL^{-1} was adequate to transform the protein-starch gel network, which was easily shaped and fixed onto the bottom of the tilted container, thus preventing blood from flowing down due to gravity.

In addition to visual observation, viscosity evaluation of the blood/MSS@Fe_2O_3 mixture was performed. As shown in Fig. 4C, phase transition started when only 300 mg mL^{-1} of MSS@Fe_2O_3 was applied because the viscosity drastically increased to 4321 Pa s. Further rheological results, namely the elastic (G′) and viscous (G″) moduli of the mixtures, are shown in Fig. 4D. With an increase in particle concentration, both the corresponding G′ and G″ values increased in all test

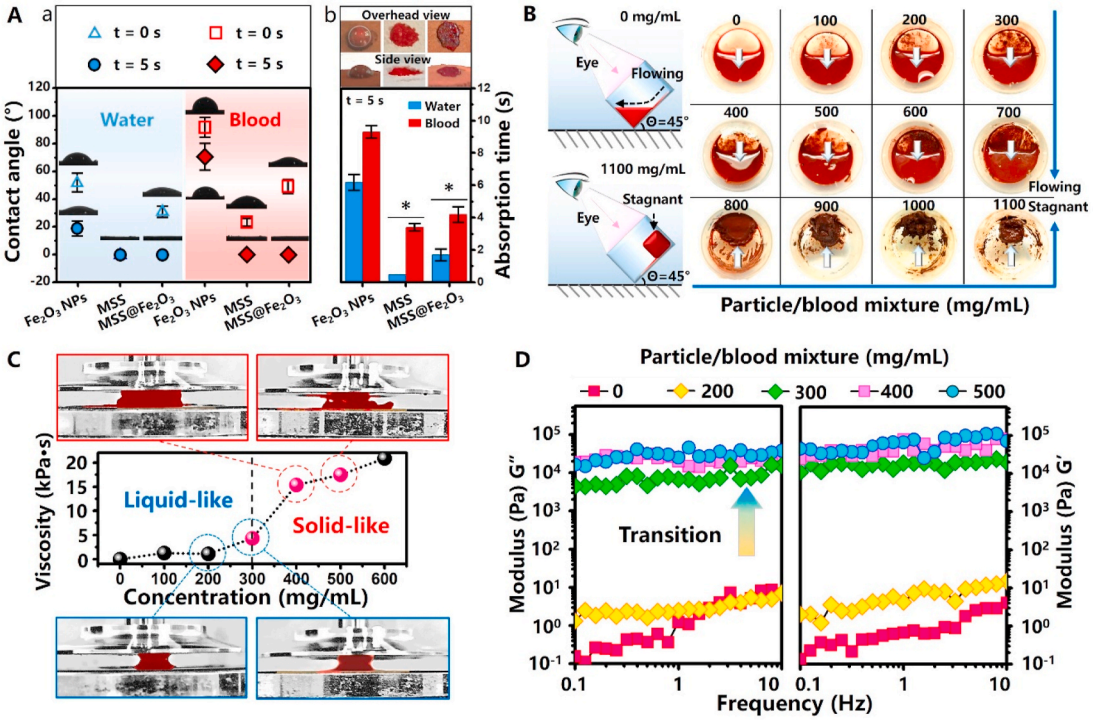

Fig. 4. A) a) Contact angles of water and blood on Fe_2O_3 NPs, MSS, and MSS@Fe_2O_3 and b) the corresponding absorption time. Insets are the full-scale images of liquid absorbed by the samples. *$p < 0.05$. B) Schematic and photographs of the blood/MSS@Fe_2O_3 mixtures in a tilted container. C) Viscosity of the blood/MSS@Fe_2O_3 mixture. D) Elastic modulus (G′) and viscous modulus (G″) of the blood/MSS@Fe_2O_3 mixture.

frequency ranges. A distinct increase in both G′ and G″ values was detected at 1 Hz from concentrations of 300 mg mL^{-1} (G″ = 18839.4 Pa; G′ = 6754.2 Pa), confirming the transition of the particle/blood mixture from liquid-like (G′ < G″) to solid-like (G′ > G″) structures. Notably, the concentration of the mixtures determined the stability of the blood clot. When the MSS@Fe_2O_3 dosage reached a critical point, blood solidified immediately and a solid-like structural barrier was observed owing to the excellent hemotropic and gelation properties of MSS@Fe_2O_3, resulting in blocked blood flow from the wound.

Assessment of Blood Coagulation Mechanisms. Although MSS@Fe_2O_3 demonstrates hemostasis performance owing to the excellent physical properties of MSS, the typical hemostatic drug thrombin was further loaded on MSS@Fe_2O_3 to facilitate enhanced hemostasis (mass of thrombin over MSS@Fe_2O_3-T was 7.64 U/g). In the loading procedure (preparation of MSS@Fe_2O_3-T by loading thrombin over MSS@Fe_2O_3), the utilization efficiency of thrombin over MSS@Fe_2O_3-T and MSS were respectively 76.4 ± 4.7% and 81.5 ± 3.8% (Fig. S5), suggesting a high affinity between thrombin and the carrier (MSS@Fe_2O_3 and MSS). This high affinity indicated that thrombin was firmly fixed to the carrier to activate blood coagulation for hemostasis. The *in vitro* blood clotting capacity of MSS@Fe_2O_3-T was measured and compared with that of MSS and MSS@Fe_2O_3. As shown in Fig. 5A and B, the formation of Fe_2O_3 aggregates over MSS resulted in a prolonged blood clotting time (253.2 ± 21.4 s) compared with that of MSS (183.7 ± 23.6 s), which may be ascribed to the sacrifice of porosity of MSS during the loading of Fe_2O_3 NPs as mentioned earlier. The loading of thrombin substantially enhanced the coagulation capacity of MSS@Fe_2O_3, and the corresponding clotting time of MSS@Fe_2O_3-T was as short as 82 ± 17.2 s. As this clotting time was shorter than that of pure thrombin (108 ± 19.4 s), it could be inferred that MSS@Fe_2O_3 could enhance the hemostasis of thrombin. The enhanced hemostatic performance of MSS@Fe_2O_3-T may be a result of the negatively charged surface of MSS in MSS@Fe_2O_3-T. The negative potential endowed MSS with the ability to activate RBCs and platelets, thereby contributing to blood coagulation [36]. Thus, compared with pure thrombin, thrombin in MSS@Fe_2O_3-T was able to clot blood much faster because of the coexistence of negatively charged MSS. As shown in Fig. 5B(b), the blood clot ratio increased rapidly in the presence of MSS@Fe_2O_3-T with time, suggesting that the blood coagulative actions of MSS@Fe_2O_3-T were time-dependent. Further measurements were conducted to investigate the blood coagulation mechanisms. Fig. 5C shows the absorbance of free red blood cells (RBCs) and the aggregated numbers of platelets. Low absorbance values of free RBCs and high aggregated numbers of platelets are indications of efficient cell aggregation capacity; therefore, the hemostatic performance of MSS@Fe_2O_3-T was superior to those of MSS and Fe_2O_3 NPs. As shown in Fig. 5D, MSS@Fe_2O_3-T aided the aggregation of RBCs and the adherence of platelets to the surface or pores of MSS. In addition, fibrin piled over the MSS@Fe_2O_3-T particles, contributing to the construction of a three-dimensional MSS@Fe_2O_3-T/blood cells/fibrin network for blood clots. In general, the high negative potential surface of MSS in MSS@Fe_2O_3-T could play an important role in blood clotting. It was observed that the loading of thrombin on MSS@Fe_2O_3 slightly decreased the zeta potential of MSS@Fe_2O_3 (Fig. 5E); however, the potential was confirmed to be sufficient to activate platelets (Fig. 5C and D). Furthermore, thrombin in MSS@Fe_2O_3-T promoted the formation of fibrin from fibrinogen. Compared to the control, unaltered prothrombin time (PT) values and decreased activated PT time (APTT) values revealed that blood coagulation was stimulated by the intrinsic coagulation pathway (Fig. 5F), regardless of the materials, of which MSS@Fe_2O_3-T showed the lowest APTT value, suggesting its best potential in blood coagulation. This process can be summarized in three steps (Fig. 5G). First, after contact with blood, MSS@Fe_2O_3-T aggregated RBCs and platelets due to its excellent hemotropic properties and high porosity; then, the negatively charged surface of MSS@Fe_2O_3-T acted synergistically with the intrinsic coagulation pathway to promote the activation of platelets, thereby initiating the coagulation process; finally, thrombin from MSS@Fe_2O_3-T accelerated the formation of fibrin, contributing to blood clotting.

Examination of Dispersion Behavior of MSS@Fe_2O_3-T-$NaHCO_3$. Extensive hemorrhage typically occurs in wounds with winding and

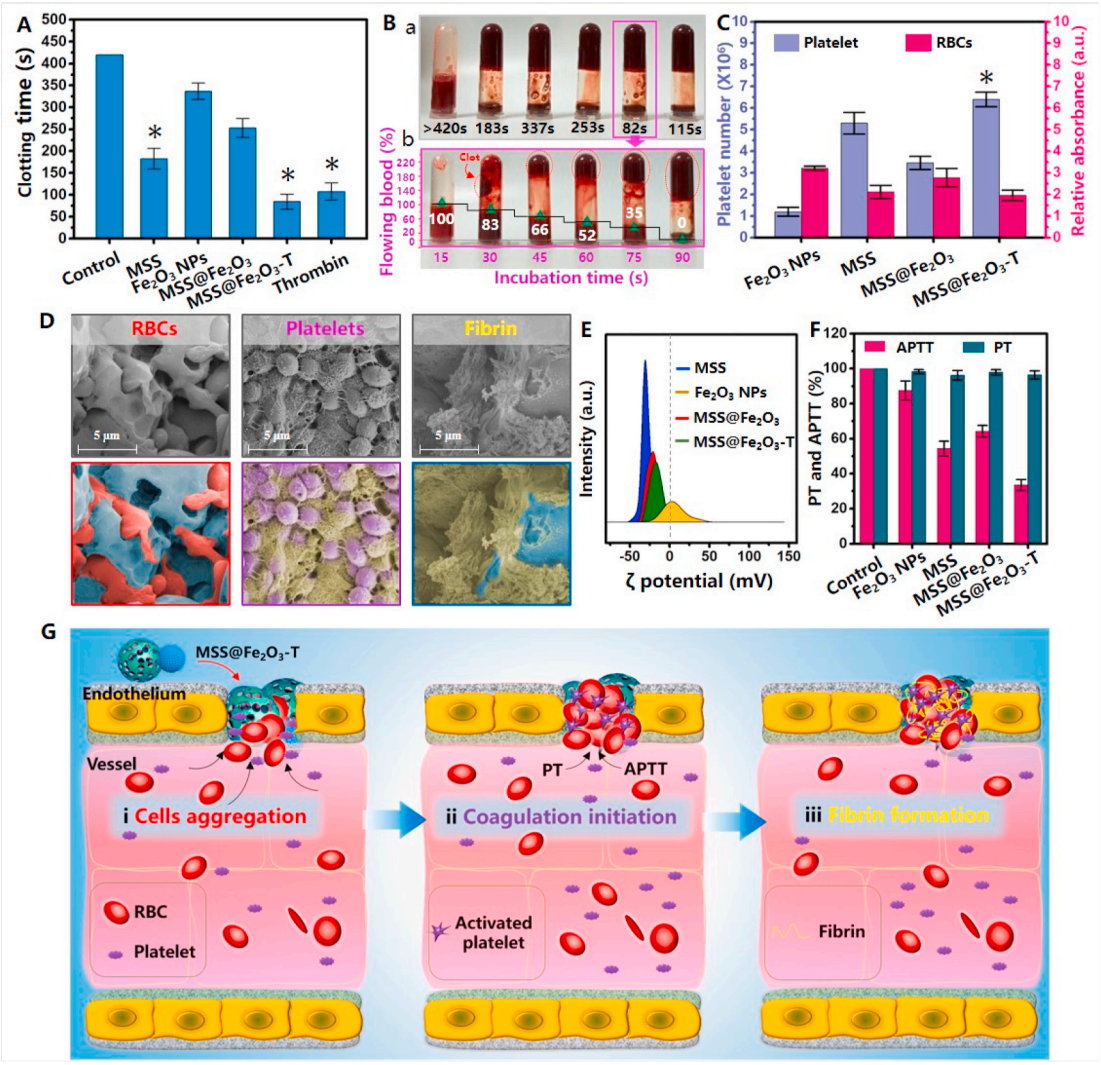

Fig. 5. A) Clotting time in whole blood. *p < 0.05. B) Photographs of a) blood clotting (from left to right: control, MSS, Fe_2O_3, MSS@Fe_2O_3, MSS@ Fe_2O_3-T, and thrombin) and b) blood clot ratio for MSS@ Fe_2O_3-T. C) Platelet and RBC aggregation assays. *p < 0.05. D) Scanning electron microscopy images for RBCs, platelets, and fibrin treated with MSS@Fe_2O_3-T. The blue, red, purple, and yellow colors represent MSS@Fe_2O_3-T, RBCs, platelets, and fibrin, respectively. E) PT and APTT assays. F) Zeta potential. G) Schematic of the proposed hemostatic mechanisms of MSS@ Fe_2O_3-T.

ramiform enterocele, which may obscure broken blood vessels. In general, particle hemostatic agents are easily aggregated and therefore may lack sufficient contact with blood when applied onto wounds [37,38], resulting in a weak blood-clotting barrier that poorly resists rushing blood or barely forming any blood-clotting barrier to block fast-flowing blood. Additionally, poor dispersion of particle hemostatic agents in blood may lead to a deficiency of the particles in some of the bleeding sites, which substantially decreases the effectiveness of the hemostatic agents. In light of this, a self-dispersion strategy relying on bubble propulsion was proposed for MSS@Fe_2O_3-T to increase its dispersibility in blood. To begin with, a modified Janus particle (MSS@Fe_2O_3-T--$NaHCO_3$) was first prepared with a core-shell structure in which the MSS@Fe_2O_3-T core was wrapped with a $NaHCO_3$ shell using the freeze-drying method (Fig. 6A). $NaHCO_3$ temporally blocked the surface pores on MSS (Fig. 6B) and wrapped MSS@Fe_2O_3-T completely (Fig. 6B and C). Then, MSS@Fe_2O_3-T-$NaHCO_3$ (the mass percentage of $NaHCO_3$ in MSS@Fe_2O_3-T-$NaHCO_3$ was 9.1% and the mass of thrombin over MSS@Fe_2O_3-T-$NaHCO_3$ was 6.95 U/g) was doped with protonated tranexamic acid (TXA-NH_3^+) particles to establish an acidic environment in blood, which facilitated the coexisting MSS@Fe_2O_3-T-$NaHCO_3$ to generate bubbles (CO_2 gas) for the rapid self-dispersion of MSS@Fe_2O_3-T. Fig. 6D and movie S7 show the dispersion behavior of MSS@Fe_2O_3-T-$NaHCO_3$, with the aid of TXA-NH_3^+, in the model mimicking forked and covert wounds (Fig. S6). MSS@Fe_2O_3-T exhibited poor dispersion in the water system and accumulated at the tip-end of wedge-shaped Channels A, B, and B′ due to magnetic field mediation. In comparison, the dispersion of $NaHCO_3$-wrapped MSS (MSS-$NaHCO_3$) and MSS@Fe_2O_3-T-$NaHCO_3$ was quite different. TXA-NH_3^+ enabled the *in situ* generation of numerous CO_2 bubbles by $NaHCO_3$-containing particles (Fig. S7), which propelled MSS (converted from MSS-$NaHCO_3$) or MSS@Fe_2O_3-T (converted from MSS@Fe_2O_3-T-$NaHCO_3$) to achieve extensive self-dispersion in 5 s upon contact with water. The magnet was applied at 5 s, which guided MSS@Fe_2O_3-T (converted from MSS@Fe_2O_3-T-$NaHCO_3$) to accumulate at the tip-end of Channels A, B, B′, C, and C' at 15 s, while MSS (converted from MSS-$NaHCO_3$) was distributed in the model entirely and evenly after 15 s. As covert bleeding sites are mainly distributed in the tip-ends of the wound channels, poor accumulation of hemostatic agents in the wedge-shaped channels of wounds may decrease hemostasis effectiveness. Expectedly, the combination of magnetic guidance and bubble propulsion endowed

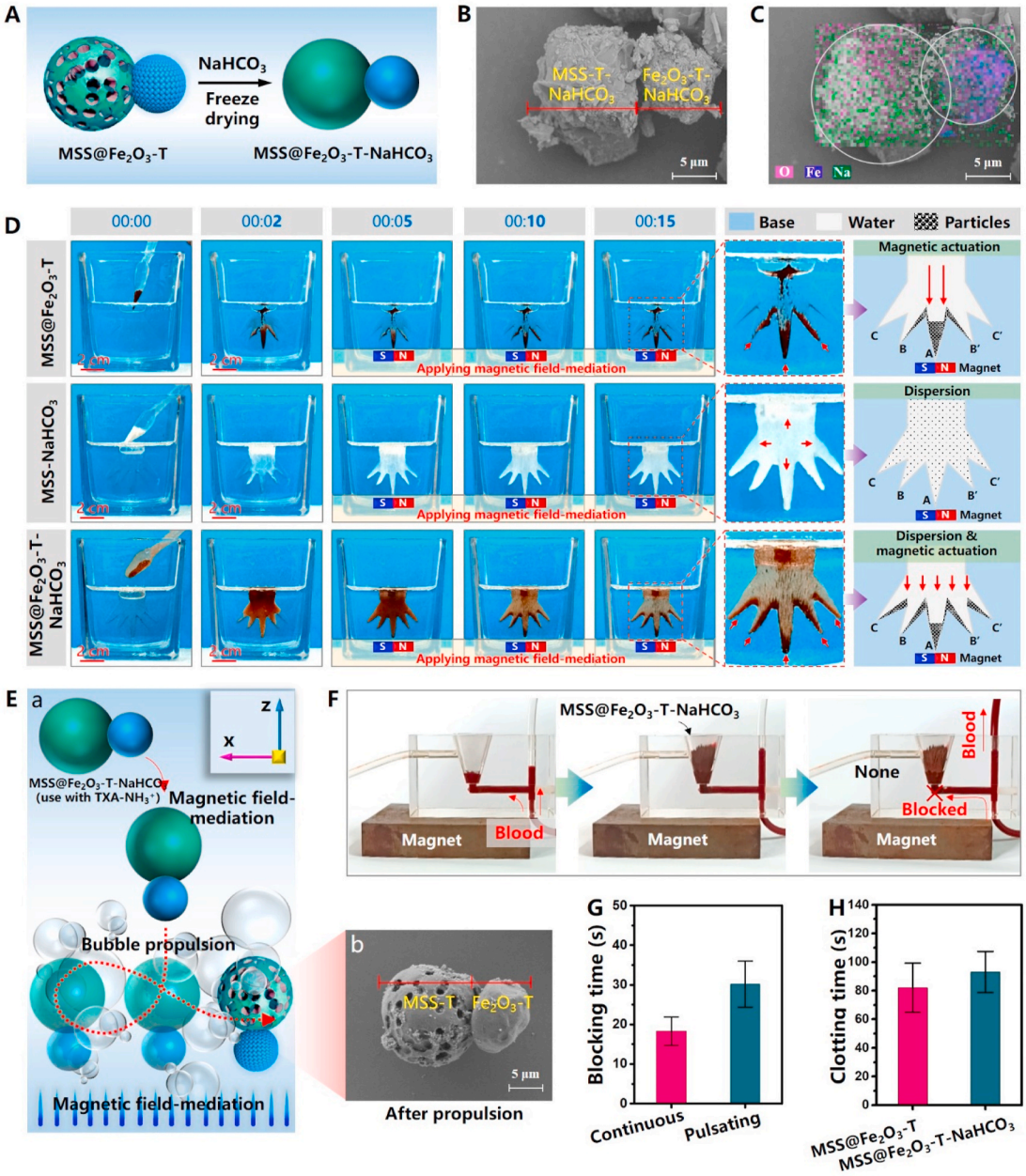

Fig. 6. A) Schematic of the preparation of MSS@Fe_2O_3-T-$NaHCO_3$. B) Scanning electron microscopy (SEM) image of MSS@Fe_2O_3-T-$NaHCO_3$ and C) the corresponding mapping image. D) Photographs of the dispersion behavior and the corresponding schematic. E) a) Schematic of the bubble propulsion behavior of MSS@Fe_2O_3-T-$NaHCO_3$ with magnetic field-mediation and b) SEM image of the particles after bubble propulsion. F) Blood-blocking behavior in the self-constructed hemorrhage model. G) Blocking time. H) Whole-blood clot assay.

MSS@Fe_2O_3-T-$NaHCO_3$ with premier drug-delivery performance in the liquid system. MSS@Fe_2O_3-T-$NaHCO_3$ first reacted with TXA-NH_3^+ to release $NaHCO_3$, leaving the bare MSS@Fe_2O_3-T, which was propelled by CO_2 bubbles to fully disperse in the liquid instantly; following magnetic actuation, MSS@Fe_2O_3-T drove and accumulated at the targeted sites according to the magnetic guidance [Figures E(a)]. It has to be pointed out that, in the process of wrapping MSS@Fe_2O_3-T with $NaHCO_3$ to prepare MSS@Fe_2O_3-T-$NaHCO_3$, $NaHCO_3$ did not affect the morphology of MSS@Fe_2O_3-T [(Fig. 6E(b)], implying that the self-dispersity strategy proposed for MSS@Fe_2O_3-T barely impacted its performance.

Supplementary data related to this article can be found at https://doi.org/10.1016/j.bioactmat.2021.05.006.

This can be supported by the fact that MSS@Fe_2O_3-T-$NaHCO_3$ exhibited good blood blocking properties (Fig. 6F), which is equivalent to that of MSS@Fe_2O_3 (Fig. 3F); similarly, the blood-blocking time of MSS@Fe_2O_3-T-$NaHCO_3$ against continuous and periodic blood flow (Fig. 6G) was also in good agreement with that of MSS@Fe_2O_3 (Fig. 3G). Furthermore, the blood clotting times of MSS@Fe_2O_3-T before and after $NaHCO_3$ loading were 82 ± 17.2 s and 93 ± 14.4 s, respectively (Fig. 6H), further suggesting that the self-dispersion strategy barely impacted blood coagulation. Thus, the self-dispersion strategy was critical for MSS@Fe_2O_3-T to avoid aggregation in blood, which may lead to decreased utilization of the dosed particle hemostatic agents; meanwhile, this wound not sacrifice the blood coagulation property of MSS@Fe_2O_3-T.

Assessment of Hemostatic Capacity in an *In Vivo* Bleeding Model. Hemorrhage that occurs in perforating and inflected wounds is difficult to control by conventional methods due to the location of deep bleeding sites and rapid blood flow. To investigate the hemostatic

capacity of MSS@Fe_2O_3-T-$NaHCO_3$ in stopping complex hemorrhage, two hemorrhage models with perforating and inflected wounds were constructed. A deep and perforating bleeding model with a "V"-shape wound was created in the femoral artery of rabbits (Fig. 7A and Movie S8). Rapid blood rushed out from the "V"-shaped wound in the femoral artery. Hemostatic particles were then applied. The use of gauze/thrombin failed to stop femoral artery bleeding (Fig. 7C). Celox™ successfully controlled severe hemorrhage over 316 ± 25 s, which was significantly longer than the time taken by MSS@Fe_2O_3-T. By simply applying the magnet right below the bleeding models, MSS@Fe_2O_3-T achieved a short hemostatic time of 237 ± 18 s, which was 11% lower than that of MSS@Fe_2O_3-T without magnetic field mediation (266 ± 24 s). The generation of bubbles, promoted by TXA-NH_3^+, was predicted to shorten the bleeding time to 206 ± 12 s for MSS@Fe_2O_3-T-$NaHCO_3$ (mass of thrombin over MSS@Fe_2O_3-T-$NaHCO_3$ was 6.95 U/g). When applied concurrently with magnetic field mediation, the hemostasis time was shortened to less than 3 min (168 ± 13 s), suggesting that magnetic field-mediated MSS@Fe_2O_3-T-$NaHCO_3$ was able to control perforating and severe hemorrhage. Additionally, to evaluate the hemostatic capacity of MSS@Fe_2O_3-T-$NaHCO_3$ against inflexed bleeding wounds, an inflected bleeding model with a "J"-shaped wound was created in the rabbit liver (Fig. 7B). Relative to that of the controls, the time taken to stop bleeding was the shortest for MSS@Fe_2O_3-T-$NaHCO_3$ with magnetic actuation (Fig. 7B and H).

Supplementary data related to this article can be found at https://doi.org/10.1016/j.bioactmat.2021.05.006.

Both magnetic field mediation and bubble propulsion significantly enhanced the hemostatic capacity of MSS@Fe_2O_3-T-$NaHCO_3$. In the

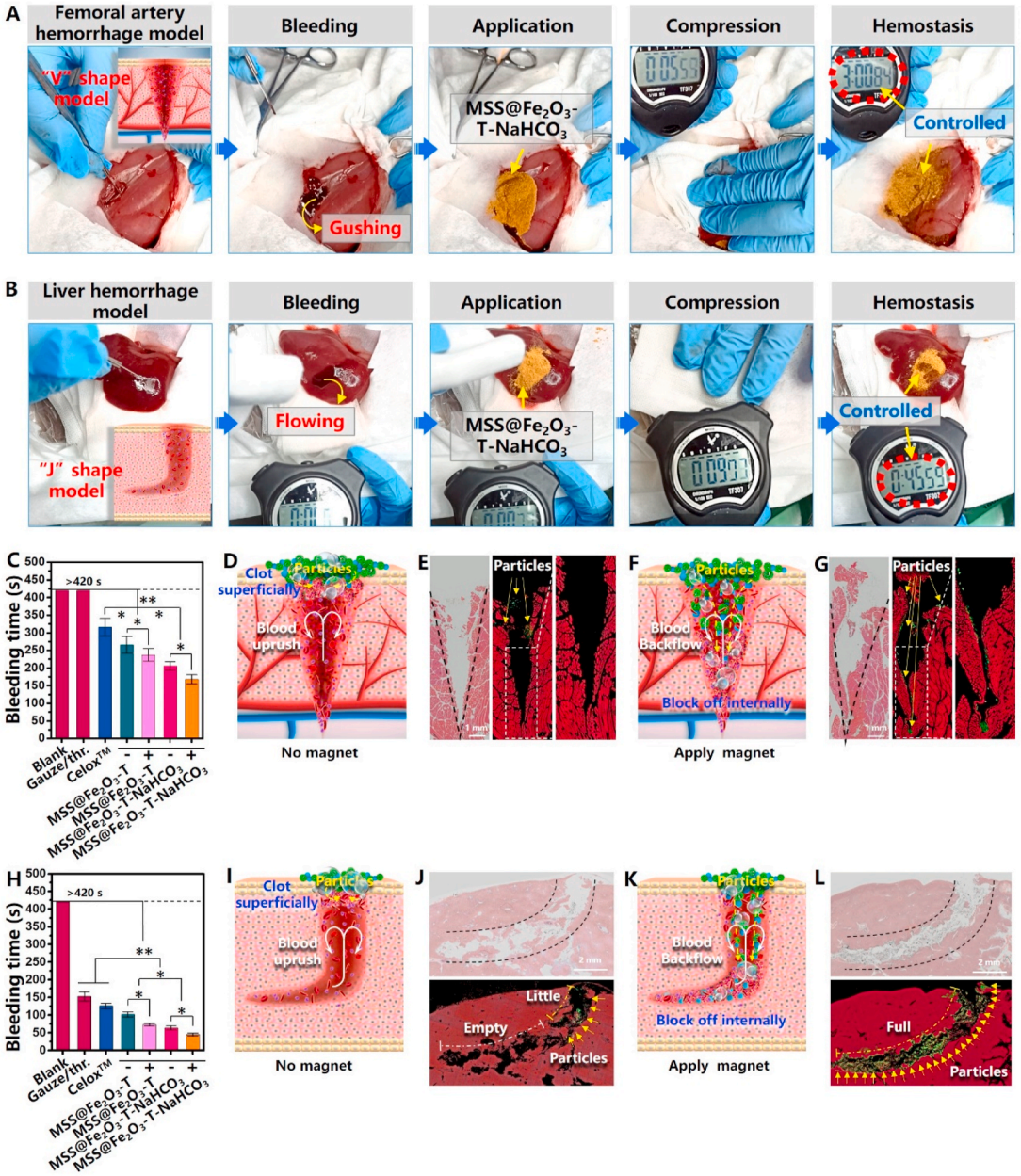

Fig. 7. Images of hemostasis in A) femoral artery and B) liver bleeding models. C) Bleeding time in femoral artery hemorrhage models. Positive and negative signs indicate the presence and absence of magnetic field mediation, respectively. *p < 0.05. D–G) Schematic depicting femoral hemorrhage models and corresponding stained tissue sections for treatment (D and E) without and (F and G) with magnetic field mediation. H) Bleeding time in liver hemorrhage models. *p < 0.05, **P < 0.01. I–L) Schematic diagram of the liver models and corresponding stained tissue sections (I and J) without and (K and L) with magnetic field mediation. Green fluorescence indicates starch particles stained with FITC. Red fluorescence indicates cells stained with Alexa Fluor 647-Phalloidin (Molecular Probes).

absence of magnetic field mediation, bubble propulsion and blood coagulation were restricted to the top or surface of the bleeding wound (Fig. 7D and I), which resulted in inefficient control of severe hemorrhage. In contrast, due to strong magnetic induction, the particles rapidly travelled and then adhered to the inside or bottom of the bleeding wound against rushing blood flow (Fig. 7F and K). Bubble propulsion occurred inwardly and promoted the extensive diffusion of particles around the bleeding site. Thus, blood coagulation at the original bleeding site may shorten hemostasis time. The effects of the magnetic field-mediated driving behavior of MSS@Fe_2O_3-T-$NaHCO_3$ on bleeding control in the "V"- and "J"-shaped models were confirmed in stained tissue sections. Fluorescein isothiocyanate (FITC)-dyed particles with green fluorescence were observed at the top and upper border of the hemocoel for "V"- and "J"-shaped wounds (Fig. 7E and J), suggesting that blood coagulation was restricted to the superficial surface of bleeding wounds without magnetic treatment. In contrast, particles were observed in the interior and at the bottom of the "V"- and "J"-shaped wounds in the presence of the magnet (Fig. 7G and L). Magnetic field-mediated MSS@Fe_2O_3-T-$NaHCO_3$ exhibited excellent adaptation even in the inflected and deep cavity of the "J"-shaped wound. The hemocoel of the "J"-shaped wound was filled with particles, confirming the high efficiency of magnetic field-mediated MSS@Fe_2O_3-T-$NaHCO_3$ in controlling inflected bleeding wounds. These results demonstrated that magnetic field mediation efficiently propelled particles into the inside and bottom of the bleeding wound against blood flow. The powerful attraction and fixation of particles in the interior or bottom of the wounds ensured the propulsion of explosive particles, and efficient blood coagulation occurred inwardly throughout bleeding sites, thereby contributing to rapid hemostasis.

Biocompatibility Assays. Good hemocompatibility and

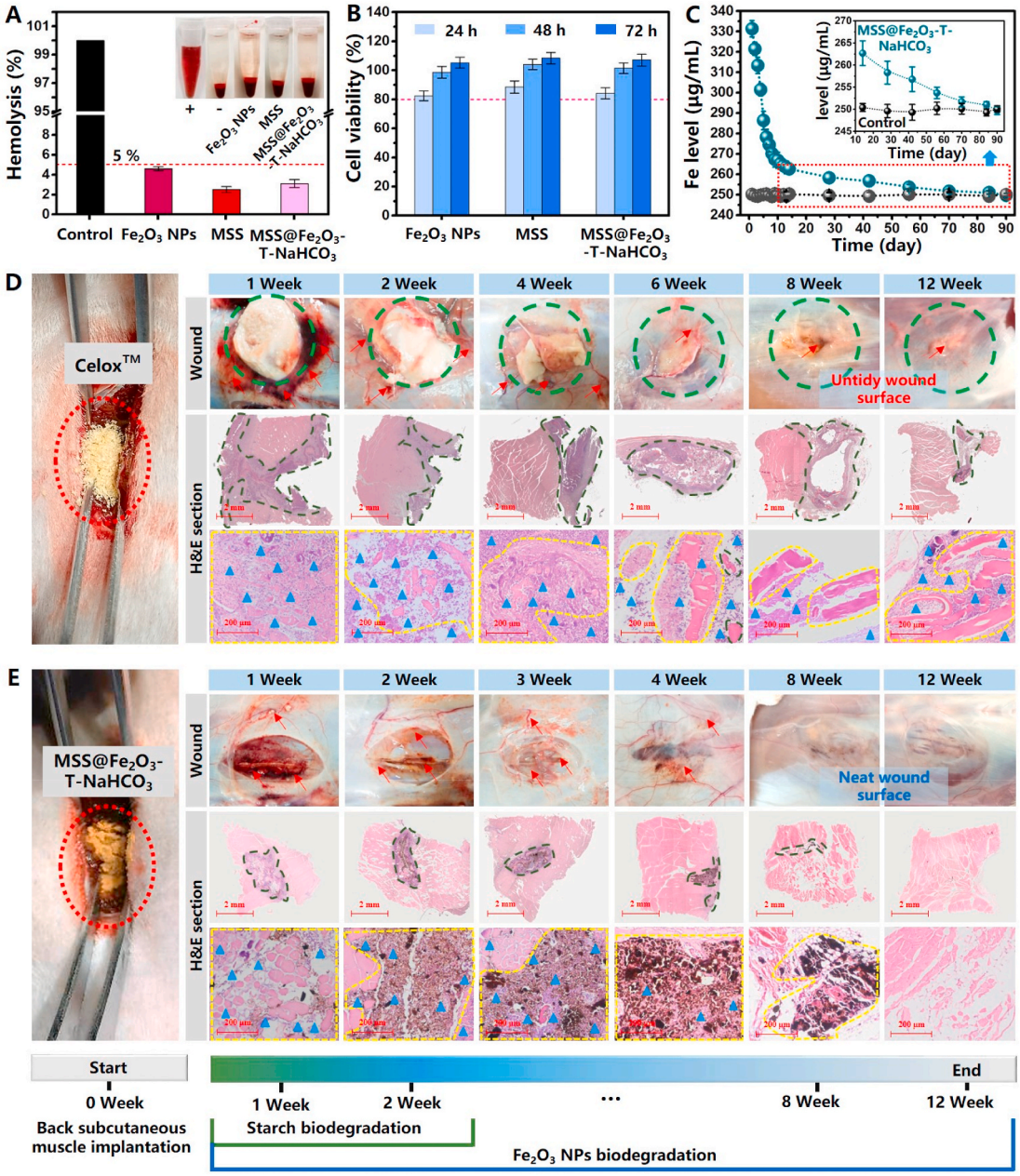

Fig. 8. A) Hemolysis assay with photographs of samples. B) Cell viability assay. C–E) Rabbit back subcutaneous muscle biodegradation models. C) Iron levels in rabbit blood treated with Celox™ and MSS@Fe_2O_3-T-$NaHCO_3$. Photographs of implantation wounds and hematoxylin and eosin (H&E)-stained sections for D) Celox™ and E) MSS@Fe_2O_3-T-$NaHCO_3$. Residues, bleeding, and inflammatory cells are depicted by dotted lines, red arrows, and blue triangles, respectively.

cytocompatibility are necessary properties of hemostatic materials [39]. A hemolysis assay and L929 cell cytotoxicity test were conducted for MSS@Fe_2O_3-T-$NaHCO_3$. The results are presented in Fig. 8A and B. A low hemolysis ratio of <5% was detected for MSS, Fe_2O_3 NPs, and MSS@Fe_2O_3-T-$NaHCO_3$ (Fig. 8A), suggesting the good hemocompatibility of these materials [40,41]. As shown in Fig. 8B, L929 cells exhibited high viability of over 80% after treatment with MSS, Fe_2O_3 NPs, or MSS@Fe_2O_3-T-$NaHCO_3$ for 24, 48, and 72 h. These results indicated the lack of cytotoxic effects on L929 cells. Good cytocompatibility was further confirmed by observing the morphology of L929 cells (Fig. S8). Live fusiform-shaped cells stained with green fluorescence filled the observation field in samples from all groups. Red signals were detected in the fluorescence microscopy images, indicating dead cells in the culture solution. These results signified the good hemocompatibility and cytocompatibility of MSS@Fe_2O_3-T-$NaHCO_3$.

The biodegradability of MSS@Fe_2O_3-T-$NaHCO_3$ was evaluated in rabbit back subcutaneous muscle biodegradation models. After implantation, the Fe levels in blood decreased over time (Fig. 8C), indicating that MSS@Fe_2O_3-T-$NaHCO_3$ was gradually biodegraded by histocytes. Higher Fe levels than those in the controls indicated ongoing metabolic reactions of Fe iron or particles. Elemental iron levels in week 12 were equal to those of the controls, suggesting the biodegradation of MSS@Fe_2O_3-T-$NaHCO_3$. In weeks 1, 2, 3, 4, 8, and 12, musculature treated with MSS@Fe_2O_3-T-$NaHCO_3$ or Celox™ was photographed and excised for histological analysis. As shown in Fig. 8D, Celox™ swelled after implantation and was released with blood from the sutural muscle wound, forming large foreign matter, which may have caused a severe inflammatory response. Swollen Celox™ still covered the surface of the muscle wound at 12 weeks after implantation, indicating poor biodegradability of Celox™ after 12 weeks. The poor biodegradability of Celox™ was confirmed in hematoxylin and eosin (H&E)-stained sections, and Celox™ residue was observed in stained sections at 12 weeks. Inflammatory cells were observed in all histological sections, confirming that Celox™ caused severe inflammation. In contrast, MSS@Fe_2O_3-T-$NaHCO_3$ exhibited good biocompatibility. The wound surface of the biodegradation models treated with MSS@Fe_2O_3-T-$NaHCO_3$ were neat and smooth (Fig. 8E). A limited amount of blood was observed on the wound surface at 1, 2, 3, and 4 weeks, which could have been due to capillary hemorrhage during the operation. The good biodegradability of MSS@Fe_2O_3-T-$NaHCO_3$ was further confirmed by images of H&E-stained muscle sections, as shown in Fig. 8E. After implantation for 1 week, small black dots connected with gray dots were observed in the histological sections, indicating MSS and Fe_2O_3 of MSS@Fe_2O_3-T-$NaHCO_3$. After 2 weeks, only the black dots were observed, suggesting the degradation of MSS in MSS@Fe_2O_3-T-$NaHCO_3$. Black fragments were observed instead of black dots, suggesting aggregation of the residual Fe_2O_3 NPs. The aggregated Fe_2O_3 NPs finally disappeared in the histological sections at 12 weeks, indicating complete degradation of MSS@Fe_2O_3-T-$NaHCO_3$. No inflammatory cell was observed in the histological sections at 8 weeks, indicating good biocompatibility of MSS@Fe_2O_3-T-$NaHCO_3$. These results revealed the excellent biodegradability of MSS@Fe_2O_3-T-$NaHCO_3$, which was completely biodegraded *in vivo* within 12 weeks.

3. Conclusion

Various strategies and materials have been designed for hemorrhage control in perforating and inflected wounds with excessive bleeding, but most of them have critical shortcomings. Here, Janus hemostatic particles (MSS@Fe_2O_3-T) with magnetic-field mediation and self-propulsion capacities were developed to tackle existing difficulties. By coordinating with $NaHCO_3$ and TXA-NH_3^+, the Janus particles self-dispersed immediately upon contact with liquids and travelled to deep perforating and inflected channels in wounds for a sustained period by magnetic guidance, after which the MSS and thrombin components synergistically stimulated blood coagulation towards hemostasis. Animal tests confirmed that these particles were versatile in hemorrhage control for "V"-shaped femoral artery and "J"-shaped liver bleeding models, with hemostasis times of 3 min and 45 s, respectively. Further assays indicated that the Janus particles had premier biocompatibility and biodegradability. This study represents the first reported trial on the use of magnetic guidance to establish hemostasis for perforating and inflected wounds. Magnetic field derived from magnets has been used in many reports in bioengineering. The merits of magnets, such as simplicity in use, the portability for carrying and the customizability in shape/volume, ensure that they could be equipped in the first aid kits feasibly and easily for emergency lifesaving. The sustained magnetic guiding strategy closed the gap between the hemostatic particles and the bleeding channels in perforating and inflected wounds. Therefore, the prepared MSS@Fe_2O_3-T-$NaHCO_3$ Janus particles are anticipated to contribute to favorable outcomes in prehospital treatments and surgical procedures by promptly establishing hemostasis.

4. Materials and methods

4.1. Agents and animals

Natural corn starch (NS), α-amylase (100 U mg^{-1}), and glucoamylase (100 U mg^{-1}) were obtained from Sigma-Aldrich (Shanghai, China). Prothrombin time (PT) and activated PT time (APTT) kits were purchased from Jingen Biotechnology Co., Ltd (Beijing). All the other chemicals used were commercially available. New Zealand white rabbits, obtained from the Animal Laboratory Center of Third Military Medical University of China, were used to obtain blood and to create the animal models. Animal care and all animal experiments were approved by the National Center of Animal Science Experimental Teaching of Southwest University of China and were performed in accordance with the Guidelines for the Care and Use of Laboratory Animals of the National Institutes of Health of the United States.

4.2. Preparation of MSS@Fe_2O_3-T

α-Fe_2O_3 nanoparticles (Fe_2O_3 NPs) were synthesized using standard protocols according to the method reported by Tang et al. [33]. Negatively-modified-microporous starch (MSS) was synthesized as described in our previous reports [30]. A simple magnetic field-guided assembly method based on a modified sol-gel method was used to prepare the MSS@Fe_2O_3 particles. The preparation involved Fe_2O_3 NPs, MSS (0.1 g), and CTAB (0.0729 g). The final concentrations of Fe_2O_3 NPs were varied, and the mass ratios of MSS to Fe_2O_3 NPs in [MSS/Fe_2O_3] were set to 1:0.1, 1:0.5, 1:1, and 1:2. The magnetic field-guided assembly was conducted using fixed magnetic stirring at 1000 rpm. Briefly, 10 mL of the MSS/CTAB mixture and 10 mL of the Fe_2O_3 NPs/CTAB slurry were first prepared by ultrasonic dispersion. The Fe_2O_3 NPs/CTAB mixture was then added dropwise into the MSS/CTAB mixture within 5 min. The slurry was mechanically stirred at 1000 rpm at 50 °C for another 5 min, followed by magnetic stirring at 50 °C for 1 h. The sol-gel system was then incubated at 25 °C for 12 h with magnetic field guidance. The collected precipitate was washed three times with alcohol/NH_4NO_3 (10 mg mL^{-1}) to remove CTAB and dissociate Fe_2O_3 NPs. MSS@Fe_2O_3 was finally obtained by drying the residual particles under vacuum at 50 °C for 48 h.

To obtain thrombin-assembled particles (MSS@Fe_2O_3-T), MSS@Fe_2O_3 particles were mixed with the Na_2HPO_4-citric acid buffer containing bovine thrombin (10 U/1 g dry MSS@Fe_2O_3 powder). After incubation at 4 °C for 1 h, the slurry was washed with PBS and vacuum filtrated at 4 °C to remove the unentrapped thrombin. The residue was then freeze-dried at −48 °C for 48 h to prepare thrombin-loaded MSS@Fe_2O_3-T. The utilization efficiency of thrombin was detected via the thrombin color substrate assay, according to our previous method [30]. Fluorescein isothiocyanate (FITC)-stained MSS@Fe_2O_3-T was prepared for further use as described in our previous report [16].

4.3. Preparation of bubble-propelling particles

To obtain $NaHCO_3$-packaged particles (MSS@Fe_2O_3-T-$NaHCO_3$), MSS@Fe_2O_3-T was mixed with the Na_2HPO_4-citric acid buffer containing $NaHCO_3$. The mixture (0.1 g $NaHCO_3$/1 g dry starch) was freeze-dried at −48 °C for 48 h. To endow the hemostat with bubble propulsion ability, MSS@Fe_2O_3-T-$NaHCO_3$ was mixed with protonated tranexamic acid (TXA-NH_3^+) powder (the mass ratio of TXA-NH_3^+ to MSS@Fe_2O_3-T-$NaHCO_3$ was 0.171:1). TXA-NH_3^+ powder was prepared according to previously reported methods [16]. In addition, MSS packaged with $NaHCO_3$ (MSS-$NaHCO_3$) was prepared as a control using the method described above.

4.4. Characterization

A PerkinElmer NexION 300X (Parkin Elmer, USA) instrument was used to detect the Fe content for calculating the mass percentage of Fe_2O_3 NPs. The porosity of the samples was measured with an automatic mercury porosimeter (AutoPore IV 9510, USA). Magnetic measurements were performed using a vibrating sample magnetometer (VSM, LakeShore 7404, USA). XRD patterns were collected using an Ultima IV diffractometer (Nippon Science Corporation, Japan). Raman spectra were recorded using a Raman spectrometer (LabRam HR Evolution, HORIBA Jobin Yvon SAS) with 532 nm excitation. XPS measurements were performed on a PHI-5000 Versaprobe III spectrometer (ULVAC-PHI, Japan). An optical microscope (IXplore Standard, Olympus, Japan) and SEM (Quanta FEG 250, Hitachi, Japan) were used for morphological observations, and the sizes were calculated using Image J. The zeta potential measurements were conducted on a Zeta potential analyzer (Zetasizer Nano, Malvern Instruments, Ltd., UK).

4.5. Examination of Magnetic Field-mediated motion behavior

To evaluate the magnetic field-mediated motion behavior of MSS@Fe_2O_3, an external magnet (B = 0.5 T) was used in the tests. The motion behavior in static fluids (water or citrated blood) was recorded overhead. The maximum distance for magnetic induction of the particles along the horizontal and vertical tubes (internal diameter of 4 mm) was determined. To evaluate the ability of the particles to move against flowing blood, a self-constructed fluid-propelling device based on previous research was used [16]. Tubes with flowing blood were fixed horizontally and vertically to detect the maximum magnetic-responsive distance. The blood flow speeds were set from 0 to 20 cm s^{-1}. The periodic impulse of blood flow was mimicked according to a previous method [27]. by setting the blood velocity to 3 cm s^{-1} and the blood impulse cycle to 3 s.

4.6. Examination of occlusion behavior in an In vitro bleeding model

To evaluate occlusion capacity, a simulative bleeding-wound device comprising an injection pump and transport tubes and mimicking the bleeding-wound mold was constructed, as shown in Fig. S4. Citrated blood was pumped into the device through a polyvinyl chloride tube (4 mm in inner diameter) from the bleeding-wound mold (polymethyl methacrylate) by microinjection (BYZ-810 T, Hunan, China). For the evaluation, a magnet was fixed below the mold to mediate the magnetic field. Particle hemostats were dosed in the device when blood was pumped in, and the blocking time of blood was then recorded. Periodic impulse evaluation was performed as described above.

4.7. Examination of Hemophagia and Rheological Properties

To evaluate the fluid absorption capacity of MSS@Fe_2O_3, a DSA100 drop shape analyzer (Krüss, Hamburg, Germany) was employed. Particles on the stage were spread out as a slab (1 × 1 × 0.3 cm). Water and citrated blood were used to detect the contact angles and absorption time. To evaluate the viscoelastic properties, namely viscosity and oscillation, a rheometer (MCR102, Anton Paar, Austria) was used. A cone plate (1°/40 mm) was chosen, and the gap was set to 100 μm. Before the evaluation, the particles were mixed with citrated blood at mixture concentrations ranging from 100 to 1100 mg mL^{-1} for the viscosity tests. The elastic modulus (storage modulus, G′) and viscous modulus (loss modulus, G″) as a function of the frequency range were measured.

4.8. Assessment of Blood Coagulation Mechanisms

To investigate the blood coagulation mechanisms, whole blood clotting, platelet and red blood cell (RBC) aggregation, prothrombin time (PT), and activated PT time (APTT) assays were evaluated as reported previously [40,41]. In the whole blood clotting assay, 0.1 g of the sample and 60 μL of 0.2 M $CaCl_2$ solution were mixed with 2 mL of citrated blood to obtain the clotting time. Thrombin in this assay was used as the positive control; the amount of thrombin added in citrated blood (2 mL) was 0.764 U, which was equivalent to the net mass of thrombin from MSS@Fe_2O_3-T (7.64 U/g).

The platelet adhesion test was conducted using the lactate dehydrogenase (LDH) method. Platelet-rich plasma (PRP, 10^8 mL^{-1}) was incubated with the samples for 30 min at 37 °C. After the free platelets were removed by washing, the adhered platelets were lysed with 0.25 mL of 1% Triton X-100 in PBS at 37 °C for 1 h. The LDH activity was determined using a kit (Sigma-Aldrich, St. Louis, MO, U.S.A.) by measuring the optical density (OD) at 490 nm; the number of aggregated platelets was calculated from the calibration curve. For the RBC aggregation test, the samples were immersed in 5% RBC suspension for 5 min at 37 °C. The free RBCs were detected using a UV–vis spectrophotometer (TU-1901, Persee Co., Beijing, China) at 520 nm. The tests were performed in triplicates.

4.9. Examination of Dispersion Behavior

To detect the dispersion behavior, a mold with a cavity and five gaps based on polyacrylamide (PAM) was constructed, as shown in Fig. S6. Briefly, after filling with water, MSS@Fe_2O_3-T-$NaHCO_3$ (with TXA-NH_3^+ powder) were applied in the mold to observe the dispersion behavior. MSS@Fe_2O_3-T and MSS-$NaHCO_3$ were used as controls. In each group, after the particles were in the mold for 5 s, the magnet was applied below the liquid system.

4.10. Assessment of Hemostatic Capacity in an In Vivo Bleeding Model

New Zealand white rabbits were used to create bleeding models for *in vivo* hemostasis evaluations. A femoral artery hemorrhage model with a "V"-shaped wound (1.5 cm in length and 1.5 cm in depth) was created according to previously reported protocols [16]. A liver hemorrhage model with a "J"-shaped wound was created according to previously reported methods [30], with modifications. Briefly, a 1-cm wide and 0.5-cm deep inflected bleeding cavity was created. Weights of 2 g and 0.5 g of MSS@Fe_2O_3-T-$NaHCO_3$ were used in each "V"-shaped and "J"-shaped severe hemorrhagic wound model, respectively. For both hemorrhage models (n = 6 for each model), a blank group, thrombin loaded gauze (gauze/thr.), Celox™, and MSS@Fe_2O_3-T-$NaHCO_3$ application without magnetic field mediation were used as controls. The dosage of thrombin loaded over gauze was 11.86 U and 2.97 U for the "V"-shaped and "J"-shaped models, respectively; FITC-stained MSS@Fe_2O_3-T-$NaHCO_3$ was further tested in the models for histological analysis of magnetic field-mediated motion behavior in hemorrhage wounds *in vivo* (n = 6 for each model).

5. Biocompatibility Assays

Biocompatibility was measured via hemolysis, cytotoxicity, and back

subcutaneous muscle implantation assays according to previously reported protocols [16,42]. The evaluated sample concentration in the hemolysis assay was 8 mg mL^{-1}. For the *in vivo* implantation assays, 0.05 g of the sample was subcutaneously implanted into the back muscle of New Zealand white rabbits. Iron content in the blood after implantation from 0 to 12 weeks was detected using a PerkinElmer NexION 300X (Parkin Elmer, USA) instrument.

CRediT authorship contribution statement

Qing Li: Investigation, Methodology, Formal analysis, Writing – original draft. **Enling Hu:** Investigation, Methodology, Formal analysis, Writing – original draft. **Kun Yu:** Formal analysis. **Mengxing Lu:** Data curation. **Ruiqi Xie:** Validation. **Fei Lu:** Writing – review & editing. **Bitao Lu:** Data curation. **Rong Bao:** Methodology. **Guangqian Lan:** Conceptualization.

Declaration of competing interest

The authors declare no conflict of interest.

Acknowledgments

This work was supported by the National Natural Science Foundation of China (No. 51703185, 51803170, and 51803171) and the Fundamental Research Funds for the Central Universities (nos. XDJK2019AC003 and XDJK2020B017).

Appendix A. Supplementary data

Supplementary data to this article can be found online at https://doi.org/10.1016/j.bioactmat.2021.05.006.

References

[1] M. Shin, S.G. Park, B.C. Oh, K. Kim, S. Jo, M.S. Lee, S.S. Oh, S.H. Hong, E.C. Shin, K. S. Kim, S.W. Kang, H. Lee, Complete prevention of blood loss with self-sealing haemostatic needles, Nat. Mater. 16 (2017) 147–152.
[2] Y. Bu, L. Zhang, G. Sun, F. Sun, J. Liu, F. Yang, P. Tang, D. Wu, Tetra-PEG based hydrogel sealants for in vivo visceral hemostasis, Adv. Mater. 31 (2019) 1901580–1901590.
[3] D.A. Hickman, C.L. Pawlowski, U.D.S. Sekhon, J. Marks &A.S. Gupta, Biomaterials and advanced technologies for hemostatic management of bleeding, Adv. Mater. 30 (2018) 1700859–1700899.
[4] S. Chen, M.A. Carlson, Y.S. Zhang, Y. Hu &J. Xie, Fabrication of injectable and superelastic nanofiber rectangle matrices ("peanuts") and their potential applications in hemostasis, Biomaterials 179 (2018) 46–59.
[5] H. Yuan, L. Chen &F.F. Hong, A biodegradable antibacterial nanocomposite based on oxidized bacterial nanocellulose for rapid hemostasis and wound healing, ACS Appl. Mater. Interfaces 12 (2020) 3382–3392.
[6] Y. Liang, C. Xu, F. Liu, S. Du, G. Li, X. Wang, Eliminating heat injury of zeolite in hemostasis via thermal conductivity of graphene sponge, ACS Appl. Mater. Interfaces 11 (2019) 23848–23857.
[7] H. Lydon, C. Hall, H. Matar, C. Dalton, J.K. Chipman, J.S. Graham, R.P. Chilcott, The percutaneous toxicokinetics of VX in a damaged skin porcine model and the evaluation of WoundStat as a topical decontaminant, J. Appl. Toxicol. 38 (2018) 318–328.
[8] C. Liu, W. Yao, M. Tian, J. Wei, Q. Song, W. Qiao, Mussel-inspired degradable antibacterial polydopamine/silica nanoparticle for rapid hemostasis, Biomaterials 179 (2018) 83–95.
[9] X. Zhao, Y. Liang, B. Guo, Z. Yin, D. Zhu, Y. Han, Injectable dry cryogels with excellent blood-sucking expansion and blood clotting to cease hemorrhage for lethal deep-wounds, coagulopathy and tissue regeneration, Chem. Eng. J. 403 (2021) 126329–126345.
[10] X. Zhao, B. Guo, H. Wu, Y. Liang &P.X. Ma, Injectable antibacterial conductive nanocomposite cryogels with rapid shape recovery for noncompressible hemorrhage and wound healing, Nat. Commun. 9 (2018) 2784–2801.
[11] Y. Fang, Y. Xu, Z. Wang, W. Zhou, L. Yan, X. Fan, H. Liu, 3D porous chitin sponge with high absorbency, rapid shape recovery, and excellent antibacterial activities for noncompressible wound, Chem. Eng. J. 388 (2020) 124169–124180.
[12] T.L. Landsman, T. Touchet, S.M. Hasan, C. Smith, B. Russell, J. Rivera, D. J. Maitland, E. Cosgriff-Hernandez, A shape memory foam composite with enhanced fluid uptake and bactericidal properties as a hemostatic agent, Acta Biomater. 47 (2017) 91–99.
[13] X. Yang, W. Liu, Y. Shi, G. Xi, M. Wang, B. Liang, Y. Feng, X. Ren, C. Shi, Peptide-immobilized starch/PEG sponge with rapid shape recovery and dual-function for both uncontrolled and noncompressible hemorrhage, Acta Biomater. 99 (2019) 220–235.
[14] Y. Wang, C. Wang, L. Qiao, J. Feng, Y. Zheng, Y. Chao, W. He, Y. Xie, W. Shuai, M. Li, Shape-adaptive composite foams with high expansion and absorption used for massive hemorrhage control and irregular wound treatment, Applied Materials Today 13 (2018) 228–241.
[15] J.R. Baylis, J.H. Yeon, M.H. Thomson, A. Kazerooni, X. Wang, A.E. St John, E. B. Lim, D. Chien, A. Lee, J.Q. Zhang, J.M. Piret, L.S. Machan, T.F. Burke, N. J. White, C.J. Kastrup, Self-propelled particles that transport cargo through flowing blood and halt hemorrhage, Science advances 1 (2015) e1500379-e1500379.
[16] Q. Li, E. Hu, K. Yu, R. Xie, F. Lu, B. Lu, R. Bao, T. Zhao, F. Dai, G. Lan, Self-propelling Janus particles for hemostasis in perforating and irregular wounds with massive hemorrhage, Adv. Funct. Mater. 30 (2020) 2004153–2004166.
[17] X. Peng, Z. Chen, P.S. Kollipara, Y. Liu, J. Fang, L. Lin, Y. Zheng, Opto-thermoelectric microswimmers, Light Sci. Appl. 9 (2020) 141–153.
[18] Y. Ji, X. Lin, H. Zhang, Y. Wu, J. Li, Q. He, Thermoresponsive polymer brush modulation on the direction of motion of phoretically driven Janus micromotors, Angew Chem. Int. Ed. Engl. 58 (2019) 4184–4188.
[19] M.J. Mitchell, M.M. Billingsley, R.M. Haley, M.E. Wechsler, N.A. Peppas, R. Langer, Engineering precision nanoparticles for drug delivery, Nat. Rev. Drug Discov. 20 (2021) 101–124.
[20] A. Espinosa, J. Reguera, A. Curcio, Á. Muñoz-Noval, C. Kuttner, A. Van de Walle, L. M. Liz-Marzán, C. Wilhelm, Janus magnetic-plasmonic nanoparticles for magnetically guided and thermally activated cancer therapy, Small 16 (2020) 1904960–1904974.
[21] M. Jeon, M.V. Halbert, Z.R. Stephen &M, Zhang. Iron oxide nanoparticles as T1 contrast agents for magnetic resonance imaging: fundamentals, challenges, applications, and prospectives, Adv. Mater. 1 (2020) 1906539–1906557.
[22] Q. Liu, Y. Duo, J. Fu, M. Qiu, Z. Sun, D. Adah, J. Kang, Z. Xie, T. Fan, S. Bao, H. Zhang, L.-P. Liu, Y. Cao, Nano-immunotherapy: unique mechanisms of nanomaterials in synergizing cancer immunotherapy, Nano Today 36 (2021) 101023–101052.
[23] S. Tong, H. Zhu &G. Bao, Magnetic iron oxide nanoparticles for disease detection and therapy, Mater. Today 31 (2019) 86–99.
[24] K.-Y. Qian, Y. Song, X. Yan, L. Dong, J. Xue, Y. Xu, B. Wang, B. Cao, Q. Hou, W. Peng, J. Hu, K. Jiang, S. Chen, H. Wang, Y. Lu, Injectable ferrimagnetic silk fibroin hydrogel for magnetic hyperthermia ablation of deep tumor, Biomaterials 259 (2020) 120299–120310.
[25] A.V. Singh, M.H. Dad Ansari, C.B. Dayan, J. Giltinan, S. Wang, Y. Yu, V. Kishore, P. Laux, A. Luch, M. Sitti, Multifunctional magnetic hairbot for untethered osteogenesis, ultrasound contrast imaging and drug delivery, Biomaterials 219 (2019) 119394–119405.
[26] Z. Wang, F. Zhang, D. Shao, Z. Chang, L. Wang, H. Hu, X. Zheng, X. Li, F. Chen, Z. Tu, M. Li, W. Sun, L. Chen, W.F. Dong, Janus nanobullets combine photodynamic therapy and magnetic hyperthermia to potentiate synergetic anti-metastatic immunotherapy, Adv. Sci. 6 (2019) 1901690–1901700.
[27] H. Xu, M. Medina-Sanchez, M.F. Maitz, C. Werner &O.G. Schmidt, Sperm micromotors for cargo delivery through flowing blood, ACS Nano 14 (2020) 2982–2993.
[28] S. Li, Q. Jiang, S. Liu, Y. Zhang, Y. Tian, C. Song, J. Wang, Y. Zou, G.J. Anderson, J. Y. Han, Y. Chang, Y. Liu, C. Zhang, L. Chen, G. Zhou, G. Nie, H. Yan, B. Ding, Y. Zhao, A DNA nanorobot functions as a cancer therapeutic in response to a molecular trigger in vivo, Nat. Biotechnol. 36 (2018) 258–264.
[29] G. Xi, W. Liu, M. Chen, Q. Li, X. Hao, M. Wang, X. Yang, Y. Feng, H. He, C. Shi, W. Li, Polysaccharide-based Lotus seedpod surface-like porous microsphere with precise and controllable micromorphology for ultrarapid hemostasis, ACS Appl. Mater. Interfaces 11 (2019) 46558–46571.
[30] Q. Li, F. Lu, S. Shang, H. Ye, K. Yu, B. Lu, Y. Xiao, F. Dai, G. Lan, Biodegradable microporous starch with assembled thrombin for rapid induction of hemostasis, ACS Sustain. Chem. Eng. 7 (2019) 9121–9132.
[31] W. Guo, W. Sun, L.P. Lv, S. Kong &Y. Wang, Microwave-assisted morphology evolution of Fe-based metal-organic frameworks and their derived Fe2O3 nanostructures for Li-ion storage, ACS Nano 11 (2017) 4198–4205.
[32] Z. Zhou, Q. Zhang, J. Sun, B. He, J. Guo, Q. Li, C. Li, L. Xie, Y. Yao, Metal-organic framework derived spindle-like carbon incorporated alpha-Fe2O3 grown on carbon nanotube fiber as anodes for high-performance wearable asymmetric supercapacitors, ACS Nano 12 (2018) 9333–9341.
[33] W. Tang, Q. Li, S. Gao &J.K. Shang, Arsenic (III,V) removal from aqueous solution by ultrafine alpha-Fe2O3 nanoparticles synthesized from solvent thermal method, J. Hazard Mater. 192 (2011) 131–138.
[34] M. Li, D. Li, Bidirectional transfer of particles across liquid-liquid interface under electric pulse, J. Colloid Interface Sci. 560 (2020) 436–446.
[35] J.Y. Liu, Y. Hu, L. Li, C. Wang, J. Wang, Y. Li, D. Chen, X. Ding, C. Shen, F.J. Xu, Biomass-derived multilayer-structured microparticles for accelerated hemostasis and bone repair, Adv. Sci. 7 (2020) 2002243–2002254.
[36] J. Lee, H.A. Lee, M. Shin, L.J. Juang, C.J. Kastrup, G.M. Go, H. Lee, Diatom frustule silica exhibits superhydrophilicity and superhemophilicity, ACS Nano 14 (2020) 4755–4766.
[37] D.S. Sánchez, D.L. Soler, J. Katuri, Chemically powered micro- and nanomotors. Angewandte chemie. Chemically powered micro- and nanomotors, Angew. Chem. 54 (2015) 1414–1444.
[38] A. DaShawn, L. Hickman Christa, D.S. Pawlowski Ujjal, Sekhon joyann marks anirban sen gupta. Biomaterials and advanced technologies for hemostatic management of bleeding, Adv. Mater. 30 (2017) 1700859–1700899.

[39] Z. Chen, L. Han, C. Liu, Y. Du, X. Hu, G. Du, C. Shan, K. Yang, C. Wang, M. Li, F. Li, F. Tian, A rapid hemostatic sponge based on large, mesoporous silica nanoparticles and N-alkylated chitosan, Nanoscale 10 (2018) 20234–20245.
[40] M. Long, Y. Zhang, P. Huang, S. Chang, Y. Hu, Q. Yang, L. Mao, H. Yang, Emerging nanoclay composite for effective hemostasis, Adv. Funct. Mater. 28 (2018) 1704452–1704461.
[41] F. Cheng, C. Liu, X. Wei, T. Yan, H. Li, J. He, Y. Huang, Preparation and characterization of 2,2,6,6-Tetramethylpiperidine-1-oxyl (TEMPO)-Oxidized cellulose nanocrystal/alginate biodegradable composite dressing for hemostasis applications, ACS Sustain. Chem. Eng. 5 (2017) 3819–3828.
[42] Y. Hong, F. Zhou, Y. Hua, X. Zhang, C. Ni, D. Pan, Y. Zhang, D. Jiang, L. Yang, Q. Lin, Y. Zou, D. Yu, D.E. Arnot, X. Zou, L. Zhu, S. Zhang, H. Ouyang, A strongly adhesive hemostatic hydrogel for the repair of arterial and heart bleeds, Nat. Commun. 10 (2019) 2060–2071.